

Article

Molybdenum Oxide Functional Passivation of Aluminum Dimers for Enhancing Optical-Field and Environmental Stability

Daniela Lorenzo ¹, Fabrizio Riminucci ², Mariachiara Manoccio ¹ , Gianluca Balestra ¹, Daniela Simeone ¹, David Maria Tobaldi ¹, Marco Esposito ¹ , Adriana Passaseo ¹, Vittorianna Tasco ¹  and Massimo Cuscunà ^{1,*} 

¹ CNR NANOTEC Institute of Nanotechnology, Via Monteroni, 73100 Lecce, Italy; daniela.lorenzo@nanotec.cnr.it (D.L.); mariachiara.manoccio@unisalento.it (M.M.); gianluca.balestra@nanotec.cnr.it (G.B.); daniela.simeone@nanotec.cnr.it (D.S.); david.tobaldi@nanotec.cnr.it (D.M.T.); marco.esposito@nanotec.cnr.it (M.E.); adriana.passaseo@nanotec.cnr.it (A.P.); vittorianna.tasco@nanotec.cnr.it (V.T.)

² Molecular Foundry, Lawrence Berkeley National Laboratory, One Cyclotron Road, Berkeley, CA 94720, USA; fabrizioriminucci@lbl.gov

* Correspondence: massimo.cuscuna@nanotec.cnr.it

Abstract: In this contribution, we present an experimental and numerical study on the coating of Al plasmonic nanostructures through a conformal layer of high-refractive-index molybdenum oxide. The investigated structures are closely coupled nanodisks where we observe that the effect of the thin coating is to help gap narrowing down to the sub-5-nm range, where a large electromagnetic field enhancement and confinement can be achieved. The solution represents an alternative to more complex and challenging lithographic approaches, and results are also advantageous for enhancing the long-term stability of aluminum nanostructures.

Keywords: aluminum plasmonic dimers; large refractive index molybdenum oxide; passivation; sub-5-nm gaps; local electric field enhancement; environmental stability



Citation: Lorenzo, D.; Riminucci, F.; Manoccio, M.; Balestra, G.; Simeone, D.; Tobaldi, D.M.; Esposito, M.; Passaseo, A.; Tasco, V.; Cuscunà, M. Molybdenum Oxide Functional Passivation of Aluminum Dimers for Enhancing Optical-Field and Environmental Stability. *Photonics* **2022**, *9*, 523. <https://doi.org/10.3390/photonics9080523>

Received: 30 June 2022

Accepted: 22 July 2022

Published: 28 July 2022

Publisher's Note: MDPI stays neutral with regard to jurisdictional claims in published maps and institutional affiliations.



Copyright: © 2022 by the authors. Licensee MDPI, Basel, Switzerland. This article is an open access article distributed under the terms and conditions of the Creative Commons Attribution (CC BY) license (<https://creativecommons.org/licenses/by/4.0/>).

1. Introduction

Plasmonic nanoparticle (NP) dimers [1–8] generating highly intense areas of electric field enhancement, named hot spots, have been playing a crucial role in various applications, such as chemical and biological sensing [9], surface enhanced Raman spectroscopy (SERS) [10–12], photocatalysis [13], and cavity quantum electrodynamics [14]. Local electric fields can be continuously enhanced by narrowing gaps until reaching the quantum tunnelling region (~1 nm) [15,16].

It has been theoretically demonstrated that the use of appropriately refractive dielectric coatings on dimers can greatly increase local electric field enhancement, with remarkable hot spots at the nanogaps [17–19]. Deng et al. demonstrated that dielectric Mie resonances can contribute to a strong light coupling effect, thus improving the light absorption when the dielectric shell has a large refractive index and becomes thick.

Thus far, NP dimers as bowtie nanoantennas were experimentally coated with Al₂O₃ film by Lin et al. [20] to increase the local electromagnetic (EM) field (E) enhancement factor (EF). They achieved a redshift of the plasmon resonance wavelength with respect to bare dimers and calculated a progressive EM field EF increase ($|E/E_0|^2 = 1300$, where E₀ is the incident EM field) in the gap, as the coating thickness increased.

Here, we experimentally use a high refractive index dielectric coating with nominal zero loss (MoO_x) on Al dimers, aiming to increase the electric field enhancement within the nanogap. We used plasma-enhanced atomic layer deposition (PE-ALD) [21,22], providing highly precise control of the thickness, very low contamination content, excellent uniformity and conformality on structured surfaces with complex shapes [23]. These benefits result

from the time-sequenced introduction of precursors inside the deposition zone, where selective and self-limiting half reactions occur on the surface. Hence, thin-film growth is determined by surface kinetics, allowing to avoid parasitic gas-phase reactions [24,25]. We performed a comparison between high (MoO_x) and low (Al_2O_3) refractive index coatings on Al bare dimers, as coupled nanodisks (NDs), to better establish the coating effect within the nanogaps. Furthermore, we performed a study on the EM field in the hot spots as a function of the initial nanogap, to guide ALD efficient dielectric coating.

We also show that MoO_x stabilizes the Al dimers upon exposure to indoor air, ensuring long-term durability. Al is a low-cost metal and, in the last decade, it started driving a great interest for nanoplasmonic-based devices operating in the UV/Vis spectral region [26,27]. Indeed, it is well-known that Al surfaces quickly oxidize when exposed to air, through the formation of a few nm thick stable amorphous layer [2,26]. This layer partially protects the metal against subsequent oxidation by preventing oxygen diffusion [26,28]. In the case of evaporated Al nanostructures that are featured by a polycrystalline nature, a number of defects, such as grain boundaries, are largely present; therefore, the native oxide layer may exhibit cracks at the junction between metal grains [29], where Al corrosion can occur [30]. Therefore, corrosion can limit the long-term durability of aluminum-based devices [31]. Owing to the large surface-to-volume ratio of plasmonic nanostructures, the corrosion phenomenon becomes even more restrictive at the nanoscale [32–35].

Consequently, novel methods to improve the long-term stability of optical properties of plasmonic nanostructures based on Al should be investigated for technological applications of practical utility.

Due to their wide use as solid propellants [36], a number of processes promoting the long-term stability of Al nanoparticles have been investigated throughout the last decades. Some organic materials have been used to stabilize aluminum NPs [37] but those coatings were found to be permeable to oxygen, thus showing poor passivation capability.

ALD and plasma-enhanced chemical vapor deposition (PE-CVD) of thin inert layers of metal oxides offer powerful alternative tools for Al corrosion protection. This is due to their ability to deposit dense layers of oxide materials with controlled nanometer thickness at the nanoscale. However, such layers were commonly used to protect flat metal surfaces, such as alumina, titania [38,39] and hafnia [40]. Therefore, a layer with conformal coverage on photonic nanostructures such as arrayed Al dimers, which is able to stabilize them in the long-term, is lacking. To this end, the proposed MoO_x coating has been demonstrated to sustain plasmonic resonances lasting over 6 months with a slight decrease in the localized surface plasmon resonance (LSPR) intensity.

Therefore, the overall benefit of using MoO_x dielectric coating is two-fold: it improves the plasmonic functionalities of Al nanogaps and boosts their chemical stability, which is favorable for the large-scale fabrication, integration and packaging of such nanostructures.

2. Experimental Section

2.1. Fabrication of Al Bare Dimers

Two-dimensional arrays (80×80 elements) of single and coupled Al NDs were realized on glass substrates by electron beam lithography (EBL), with lattice period of 350 nm and 470 nm, respectively. The substrate was first cleaned in acetone and 2-propanol. Then, a 180 nm poly(methyl methacrylate) (PMMA) layer was spin-coated at 5000 rpm and soft-baked at 180 °C for 3 min. A 2 nm thick chromium layer was thermally evaporated onto the PMMA to prevent charge effects in the electron beam writing procedure. The arrays were written by a Raith 150 system at a beam current of 34 pA and an electron energy of 30 keV. After electron exposure, the Cr layer was completely removed by a ceric ammonium nitrate-based wet etching for 20 s and rinsed in water. The exposed resist was developed in MIBK:IPA solution in a 1:3 ratio for 3 min and rinsed in 2-propanol for 1 min. After thermal evaporation of 31 nm thick aluminum, a lift-off process was performed in a mr-Rem500 remover solution (Microresist Technology, Berlin, Germany) and rinsed in 2-propanol.

After Al native oxidation (over indoor air exposure of 6 days, a time enabling an almost complete native oxidation [1]), the measured ND diameter is 120 nm and the thickness is 33 nm. Actually, by considering that the formation of the expected 3 nm thick native Al_2O_3 layer [26] consumes about 1 nm thick Al layer [2], we can estimate a height of about 33 nm for both dimers and individual NDs. In addition, the dimer gap after native oxidation resulted to be 28 nm.

2.2. Oxide Deposition by ALD

The amorphous dielectric films (MoO_x and Al_2O_3) were deposited in a PE-ALD system (SI ALD LL, SENTECH Instruments) composed by a reactor unit connected to a remote capacitive plasma (CCP) source, a load-lock for ergonomic wafer loading, a precursor cabinet, and a pumping unit consisting of a foreline dry pump and a turbomolecular pump reaching a base pressure of 10–6 mbar. It is worth noting that remote CCP source, driven by a 13.56 MHz generator, is attached to the upper flange of the reactor. During the deposition process, the substrate is placed outside the plasma generation region. The gas carrier flow for precursor pulsing was 40 sccm of ultra-high purity grade N_2 (99.999%). As metalorganic precursors, we used $(\text{NtBu})_2(\text{NMe}_2)_2\text{Mo}$ (from Strem chemicals Inc., Bischheim, France) and trimethylaluminum $\text{Al}_2(\text{CH}_3)_6$ (from Strem chemicals Inc., Bischheim, France) for MoO_x and Al_2O_3 depositions, respectively. The reactor wall temperature was kept uniform at room temperature (RT) during the film growth, the Mo cylinder was heated at 55 °C, and all the delivery lines were heated at 120 °C to prevent condensation of the precursor. The exposure time to O_2 reactant (150 sccm flow) was set at 2 s with RF power of 200 W. The pressure used during the growth process was approximately 20 Pa, whilst the temperature was kept at RT. The amorphous MoO_x was grown on arrayed Al bare dimers and arrayed Al NDs (both consisting of Al core/native Al_2O_3 shell), previously fabricated on a glass substrate. Furthermore, MoO_x and Al_2O_3 layers were deposited on p-type Si (100) wafers with a resistance of 1–30 Ohm \times cm (low doped substrates), thickness \sim 650–700 μm , and native oxide of 2.8 nm (as measured by spectroscopic ellipsometry (SE) using SiO_2 fit [41]), to retrieve their optical constants. All the substrates were pre-cleaned with acetone and isopropyl alcohol.

2.3. Optical and Scanning Electron Microscopy Characterization

The transmission spectra of arrayed dimers and NDs were recorded by using a home-made confocal scheme made by a Zeiss AxioScope A1 optical microscope connected to a spectrometer. The measures were performed in transmission configuration. The incoming light from a tungsten lamp (450–850 nm) was first focalized by a condenser with $\text{NA} < 0.1$, and then illuminated the sample from the bottom. Then, transmitted light was collected through a 40x objective lens with $\text{NA} = 0.95$. The microscope output image was collimated, collected, and reconstructed by a system of lenses on the entrance slits of a 200 mm spectrometer, equipped with a 150 lines/mm grating, and a CCD camera for measurements in the Vis/NIR spectral range. In the case of the dimer arrays, linear polarization measurements were performed. In this case, the incoming light was linearly polarized using a Carl Zeiss (400–850 nm) linear polarizer. The light transmission was calculated with respect to the light transmitted by the unpatterned substrate.

SE in the Vis/NIR range (450–850 nm) with a J.A.Woollam M-2000 system at three angles of incidence (50°, 55°, 60°) was employed to determine the thicknesses and the optical constants of the MoO_x and Al_2O_3 dielectric films on silicon substrates with native oxide on top. The model used to fit the SE data consisted of three layers: silicon for substrate [42], native silicon oxide [41,43] and dielectrics as top layer. In a simplified picture, a Cauchy model [44] was used for fitting the MoO_x [45] and Al_2O_3 [46]. The thickness was determined as the averaged value retrieved on a grid of 5 points on every sample.

In addition, the top view images of the samples were collected using a Zeiss Merlin scanning electron microscope (SEM), operating at 5 kV and low current (100 pA).

2.4. MoO_x Density Measurements

X-ray analysis was used to detect the density of MoO_x films deposited at RT by ALD through a Malvern PANalytical X'Pert Pro MRD diffractometer equipped with a fast PiXcel detector-CuK α radiation. Specular X-ray reflectivity (XRR) was used to obtain information about the density of the films. XRR measurements were recorded with an incidence angle from 0 to 4° 2θ . XRR patterns were fitted using the X'Pert Reflectivity software package; the sample model consisted of a MoO_x /native SiO_2 /Si stack with surface and interface roughness.

2.5. Finite-Difference Time-Domain (FDTD)-Based Numerical Simulation

Basically, the simulated structures consisted of arrayed Al core/native Al_2O_3 shell dimers and dielectric coated dimers consisting of mentioned Al core/native Al_2O_3 shell dimers coated by MoO_x or Al_2O_3 dielectric films. Dimer geometries were designed through 3D CAD module of FDTD Lumerical software. The Al [47], native Al_2O_3 [48] and TiO_2 [49] optical constants along with the experimental ones of MoO_x and Al_2O_3 layers, retrieved by SE, were used to numerically calculate the optical extinction and near-field EF maps in the bare and coated dimer nanostructures. Air was chosen as the background medium with a refractive index of 1, and the dimers were placed on a silica glass substrate with a refractive index of 1.446. The incident light travelled in the perpendicular direction to the surface containing the nanostructures with a polarization parallel (p-pol) and perpendicular (s-pol) to the long dimer axis. Boundary conditions were considered to be periodic in the two directions of the square lattice. Furthermore, symmetries were also considered to reduce the simulation time, by reducing the area of the unit cell to a fourth of the original one.

3. Results and Discussion

3.1. Molybdenum Oxide Functional Passivation of Al Dimers for Enhancing Optical Field

First, we focused on fabricating Al coupled NDs by EBL, with a gap of 28 nm, measured after native oxidation occurred (Figure 1a, top panel). The dimers were then coated with two consecutive depositions of 4 nm thick amorphous MoO_x each of which was performed at RT in order to avoid any shape damage induced by sample heating. Figure 1a (bottom panel) reports the MoO_x -coated dimers with a final gap of approximately 12 nm after the two MoO_x depositions. Such a value results from the excellent uniformity along with conformal coverage on structured surfaces of the ALD process. Indeed, by measuring the width of tens of narrowed gaps (by ultra-high resolution SEM), we found that the dimer gap narrows by following the following rule: final gap = initial gap – 2 × (oxide thickness). Hence, a deposition of 8 nm thick MoO_x on a 28 nm initial gap leads to a gap narrowing of 16 nm with a final gap of 12 nm.

As can be seen, the NDs exhibit a smooth surface and retain their circular shape. Then, the measured far-field extinction spectra before and after coatings were collected (Figure 1b), for transverse (s-pol) (perpendicular to the long dimer axis, see Figure 1a bottom panel) and longitudinal (parallel to the long dimer axis) polarized excitation. As can be seen, the oxide thickness affects the longitudinal polarization spectra very strongly. Here, the thicker is the oxide film, the higher is the intensity of the dimer LSPR appearing in the far-field extinction. The LSPR also redshifts by increasing the MoO_x thickness, switching from 710 nm in the bare case, to around 722 nm for 4 nm coating and to 734 nm for 8 nm MoO_x coating (Figure 1b). It is worth emphasizing that MoO_x films were deposited on thin native Al_2O_3 shell formed after Al air exposure (6 days after dimer fabrication).

Transversal polarization extinction curves exhibits a slight LSPR spectral redshift with the increase in the oxide thickness from 495 nm of bare dimers to 515 nm with 8 nm of MoO_x as an effect of the increased refractive index of the surrounding medium [17]. A slight intensity variation is observed in this case.

Furthermore, we numerically studied the concentration of EM field in the nanogap by increasing the dielectric film thickness. We considered the two case studies of dimers covered with 4 nm and 8 nm of MoO_x , respectively. The MoO_x optical constants were

properly retrieved on 8 nm thick films deposited by ALD on Si substrates, with the same growth parameters used to coat the dimers (Figure 2a, left panel), and were used as input parameters in FDTD numerical simulations. These latter operations were performed by considering a squared array of dielectric-coated Al dimers with lateral pitch of 470 nm as reported in the SEM image of Figure 1a (bottom panel).

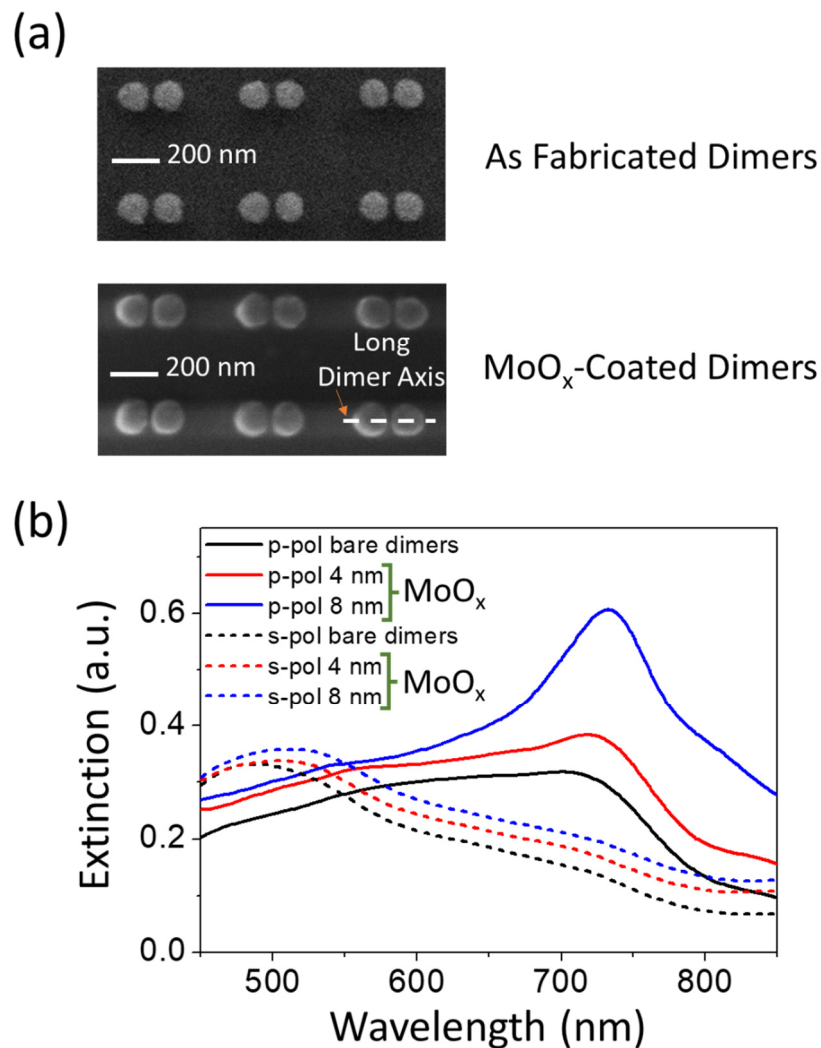


Figure 1. (a) SEM images of as-fabricated Al dimers (after native oxidation) with gap of 28 nm (top panel) and after an 8 nm thick MoO_x coating, deposited by ALD at RT, with a consequent gap narrowing down to 12 nm (bottom panel). (b) Measured optical extinction spectra of Al dimers by progressively increasing the MoO_x coating on bare nanostructures (Al core/native Al₂O₃ shell dimers) up to 4 and 8 nm thick dielectric films, for s-pol and p-pol polarized excitation.

The simulated optical extinction spectra for arrayed bare and MoO_x-coated dimers are reported in Figure S1a. Overall, they are in good agreement with the experimental measurements reported in Figure 1b. Figure 2a (right panel) demonstrates the beneficial role of the dielectric coating, which provides an enhanced optical extinction, for longitudinal polarized excitation, by increasing the oxide thickness of the MoO_x film. Such an extinction increase is accompanied by a redshift in the LSPRs from 700 nm of the Al bare dimers, to 707 and 715 nm for 4 nm and 8 nm thick MoO_x coating, respectively. On the other hand, the observed redshift in extinction resonances for longitudinal polarization could be ascribed to the increased interaction between the individual NDs as the gap is narrowed by oxide coating. Actually, when two individual metallic NPs are brought into close proximity with each other, their single surface plasmons couple themselves electromagnetically and the

resulting LSPR redshifts [12,50–52]. On the other hand, for transversal polarized excitation, we can consider non-interacting NDs in the dimer structure; hence, the LSPRs of individual NDs undergo a slight redshift (not shown) due to the resulting larger refractive index of the surrounding media, as already demonstrated in [1,2,17,53].

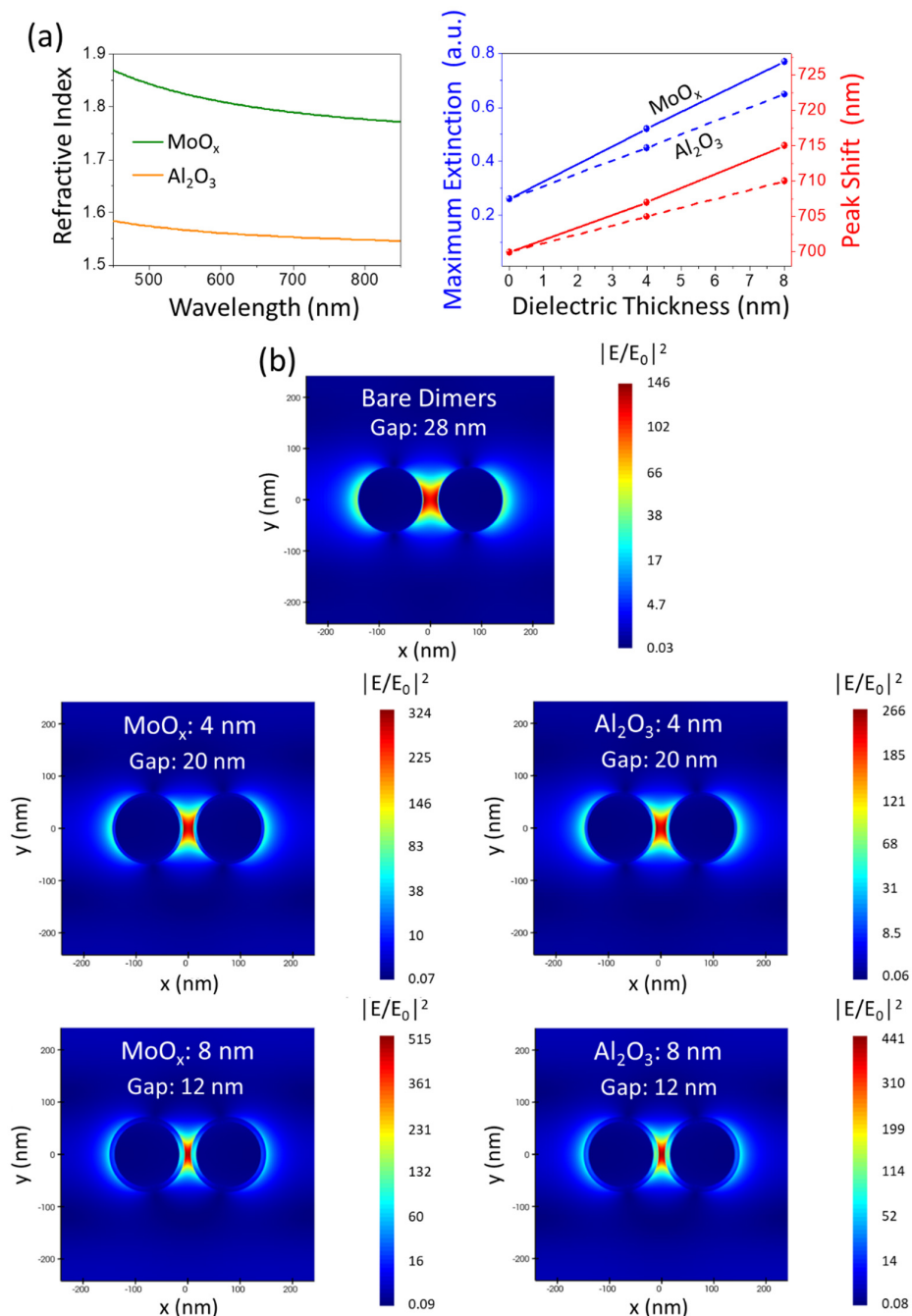


Figure 2. (a) Refractive indices of Al_2O_3 and MoO_x films, experimentally retrieved by analyzing the deposited ALD layers with SE (left panel); they were used as input parameters in FDTD numerical simulations. The extinction coefficients are null over the considered Vis/NIR spectral range. Simulated maximum extinction intensities along with peak shifts as function of the dielectric thickness (4 and 8 nm): MoO_x (solid lines) and Al_2O_3 (dashed lines) (right panel). (b) Calculated two-dimensional near-field enhancement factor $|E/E_0|^2$ ($E_0 = 1 \text{ V/m}$) maps (x-y view) for the bare (Al core/native Al_2O_3 shell dimers) and coated dimers with MoO_x and Al_2O_3 layers (4 and 8 nm thick films). The maps were extracted at corresponding wavelengths of maximum extinction peaks reported in panel a), and at the nanoantenna height where the EM field is maximum.

To better assess the effect of dielectric coating to the fabricated MoO_x-coated dimers, we extracted, in the case of longitudinal polarized excitation, the near-field maps at corresponding wavelengths of maximum optical extinction peaks reported in Figure 2a (right panel). The near-field intensity is defined as: $|E/E_0|^2$ where $|E_0| = 1$ V/m is the incident field amplitude. As can be observed in Figure 2b (for the MoO_x case), the colors indicate the $|E/E_0|^2$ values in linear scale from minimum (dark blue) to maximum (dark red); with the narrowing of the gap, the near-field maximum intensity exhibits an increase by 121% and 251% with 4 and 8 nm thick MoO_x films, respectively (from $|E/E_0|^2 = 146$ to 324 and 515 with 4 and 8 nm thick MoO_x films, respectively), as compared to as-fabricated Al dimers. The EM field is mainly concentrated in the region between the dielectric surface of the individual NDs facing each other, in agreement with our previous results concerning the effect of native oxidation on Al nanogaps [12].

Indeed, Figure S2 reports the side-view maps of the field enhancement factor $|E/E_0|^2$ of bare and MoO_x-coated dimers. As can be noted, the EM field confinement in the air gap delimited by the oxide film is highlighted. The latter also covers the glass substrate within the gap. In addition, Figure S3 shows variations in $|E/E_0|^2$ values across the nanogap of the dimers reported in Figure S2 in order to highlight the EM field confinement by progressively increasing the MoO_x coating on bare nanostructures. Figure S3 demonstrates how much the field confinement is affected by narrowing the gap, as it increases by reducing the gap size with the oxide growth.

To better establish the dielectric role, a comparison with an oxide coating characterized by a lower refractive index (in the Vis/NIR spectral range) than that of MoO_x was also addressed. To this aim, similar nanostructures were simulated with an Al₂O₃ layer, whose optical constants were experimentally retrieved on 8 nm thick films deposited by ALD on Si substrates (Figure 2a, left panel). The simulated optical extinction spectra for arrayed bare and Al₂O₃-coated dimers are reported in Figure S1b. Overall, they are in good agreement with the experimental measurements reported in Figure 1b. Roughly, as the thickness increases, the maximum extinction peak undergoes a redshift (Figure 2a, right panel), as observed for MoO_x film. However, the plasmon resonance peaks for both of the dielectric thicknesses (4 and 8 nm) have a lower maximum value with respect to the MoO_x counterparts. In addition, the near-field maps demonstrated the lower efficiency of the low refractive index Al₂O₃. As it can be observed in Figure 2b (for Al₂O₃ case), by narrowing the gap, the near-field maximum intensity exhibits a relative increase by 82% and 202% with 4 and 8 nm thick Al₂O₃ films, respectively. Such EM field EF values are lower as compared to what was obtained with the MoO_x layer.

Clearly, we can envision a very poor efficiency for dielectric layers with lower refractive indices, e.g., SiO₂, as compared to the mentioned ones.

Thanks to the rapid development of nanofabrication techniques, the production of ultranarrow metallic nanogaps is now feasible. For example, sub-10 nm gaps can be directly fabricated by high resolution electron beam lithography (EBL) or focused-ion beam (FIB) milling [54–56]. However, such direct fabrication strategies are not ideal options to fabricate sub-5 nm gaps; therefore, extremely high local field EFs [1,2] could not be easily attained. Conversely, the dielectric coating by ALD of initial nanometer-sized gaps can represent a reproducible and precise nanofabrication technique capable of producing sub-5 nm gaps. In this context, it can be of practical interest to understand the trade off between the initial gap of Al bare dimers and the maximum EM field achievable in the hot spot with the ALD dielectric coating. To shed light on that topic, a few initial Al dimer nanogaps were considered, and the EM field in the hot spot was numerically calculated by progressively narrowing the initial gaps with a dielectric coating down to a 2 nm gap. Figure 3 reports the exponential increase in the simulated EM field from $|E/E_0|^2 = 146$ up to 8063, by narrowing the Al dimer gaps from 28 nm down to 2 nm, respectively. As it can be noted, by considering a progressive MoO_x coating over three initial nanogaps of 28, 12 and 5 nm, a beneficial role of the dielectric shell is observed. This is revealed by a larger EM field enhancement within the hot spots, with respect to the initial EM field values. However, the

MoO_x-coated dimers with an initial gap of 5 nm attain large EM field values, in particular, the EM field linearly increases with a slope of 652 nm⁻¹ with respect to the values of 218 and 25 nm⁻¹ for the initial gaps of 12 and 28 nm, respectively. Furthermore, the percentage of EM field enhancement as function of the percentage of narrowed gap (by MoO_x ALD deposition), with respect to bare dimers for three initial nanogaps of 28, 12 and 5 nm, was reported in Figure S4. The latter demonstrated that the developed process is extremely efficient in the case of large initial nanogaps. Indeed, a field enhancement by more than 250% for 60% of a closed gap was attained for an initial gap of 28 nm. Conversely, a limited field enhancement (of around 50%) was obtained for the same percentage of closed gap (60%) for a narrower initial gap as low as 5 nm.

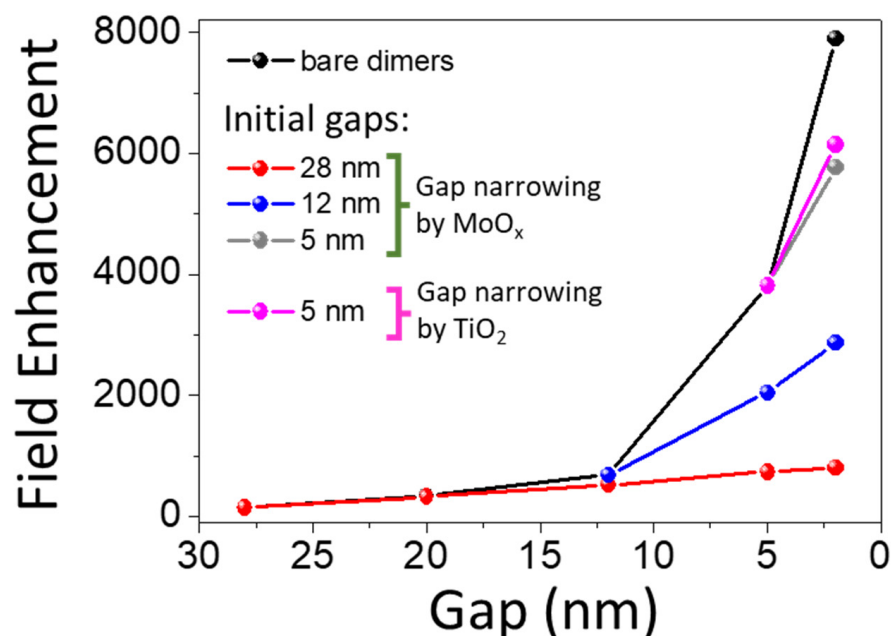


Figure 3. Maximum EM field enhancement factor $|E/E_0|^2$ ($E_0 = 1$ V/m) extracted within the dimer gaps, at corresponding wavelengths of simulated maximum extinction peaks for bare (Al core/native Al₂O₃ shell dimers) and dielectric coated dimers by progressively narrowing the initial gaps of 28, 12 and 5 nm with MoO_x layers. The EM field EF for TiO₂ (1 nm thick)-coated dimers, with an initial gap of 5 nm, is also reported. The TiO₂ film is characterized by a refractive index larger than MoO_x films in the Vis/NIR spectral range.

From the results reported in Figure 3, we clearly demonstrated the fundamental role of the initial distance between the surfaces of two metallic elements in dielectric-coated dimers. The desired $|E/E_0|^2$ reported in Figure 3 for conventional Al dimers with 2 nm gap was not attained, neither by using an initial gap of 5 nm, nor with a dielectric coating with a higher refractive index, such as TiO₂ [49] (Figure 3), with respect to the experimentally used MoO_x layer. However, pure metallic sub-5-nm gaps were obtained with complex, costly and high time-consumption technology such as He-beam lithography [2] or by EBL but only with special substrates such as thin silicon nitride membranes [57], which are capable of reducing electron backscattering effect but difficult to handle. Conversely, metallic nanogaps down to 5 nm can be prepared by using common high energy EBL (50 KeV or better 100 KeV) with high reproducibility, precision and accuracy on any substrates. Subsequently, such gaps can be furtherly narrowed down to a few nm wide gaps by leveraging the conformal coating of ALD dielectric layers. Such an approach represents a straightforward and low-cost alternative fabrication strategy to squeeze light through those nanogaps.

3.2. Molybdenum Oxide Functional Passivation of Al Dimers for Improving Environmental Stability

The dielectric coating on Al nanostructures is also relevant for their environmental stability. Many papers report the formation of a few-nm thick stable oxide layer almost immediately upon exposure to air, which preserves the nanoparticles from further degradation [2,26]. However, as demonstrated in [31], this native oxide layer partially protects the metal against subsequent oxidation; therefore, Al corrosion can occur [30].

Here, the stability of MoO_x (8 nm)-coated Al dimers, MoO_x (8 nm)-coated Al NDs and Al bare NDs arrays after being exposed to indoor air conditions (air-conditioned dark lab, 45% relative humidity at 21 °C) was evaluated by electron microscopy and optical extinction measurements. It is worth emphasizing that Al samples were stored far from chemical sources and possible contaminants in order to avoid biasing the experimental results. The samples were continuously exposed to indoor air for six months, and we did not perform periodical characterizations to induce morphology changes by sample handling, external chemical contaminations, photocorrosion [58] and electron irradiation from SEM.

Figure 4c (left panel) shows that Al bare NDs undergo an impressive morphology change along with a fractional loss of metallic matter. With respect to freshly fabricated NDs (Inset of Figure 4c, left panel), each nanodisk of the array shattered into smaller pieces. Such a change in the ND morphology results is deleterious for the plasmonic properties of those Al nanostructures because it leads to an increase in surface scattering loss with a significant decrease in the intensity of the LSPR and a huge broadening, as is clearly reported in Figure 4c (right panel). Such results are in good agreement with the results reported in [31], in which Zhang et al. observed that the optical properties of Al ND arrays are preserved for 90 days when stored in ambient air, regardless of their diameter, due to a very slight oxidation during this range of time. Over the following months, the nanodisks lose their optical properties. Conversely, the MoO_x-coated dimers and NDs remain almost unaffected in terms of morphology after being exposed for six months to indoor air (Figure 4a,b, left panels). As it can be seen, the surface of the NDs appeared smooth and retained their circular shape. This did not happen to bare Al NDs after being exposed to air for similar periods of time (see Figure 4c, left panel). After six months of air exposure, the MoO_x-coated nanostructures showed a robust preservation of the initial plasmonic properties in terms of LSPR wavelength, line width and resonant peak intensity (Figure 4a,b, right panels); only a faint LSPR intensity reduction and redshift was appreciable. This suggests that MoO_x coating, deposited by ALD, ensures long-term durability, which could be ascribed to the greatly improved performance of the physical barrier driven by a high-density material produced by PE-ALD. Actually, by means of X-ray reflectivity (XRR), we measured 3.2 g/cm³ for the MoO_x film deposited at RT, a value that can be easily improved by increasing the deposition temperature [59]. In addition, the ALD technique provides a highly conformal coverage on structured surfaces, thus avoiding air exposure of any portion of the covered Al nanostructures.

Therefore, we can envision a long-term durability of the plasmonic properties of Al nanostructures whatever their shapes are, by using conformal MoO_x coatings obtained by a powerful tool such as the ALD.

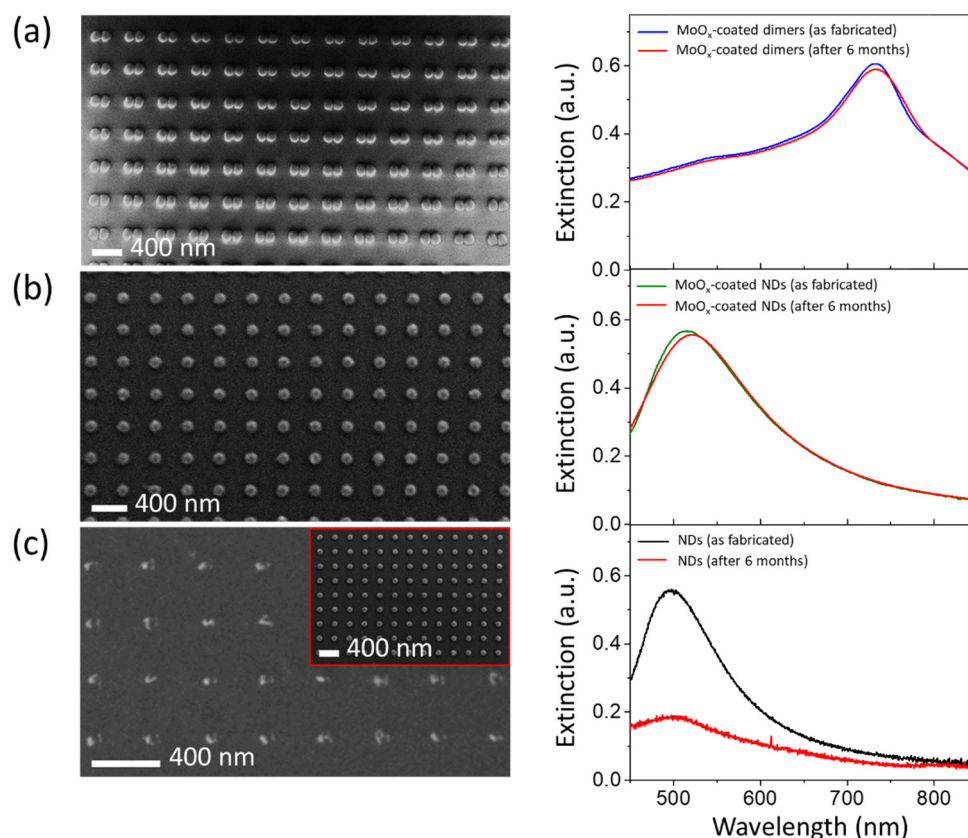


Figure 4. SEM images (left panels) and measured optical extinction spectra (right panels) of arrayed (a) MoO_x-coated Al dimers, (b) MoO_x-coated Al NDs and (c) Al NDs. The SEM images in panels (a) and (b) report the nanostructures after being exposed for 6 months to indoor air at ambient conditions (air-conditioned dark lab, 45% relative humidity at 21 °C). The SEM images in panel (c) report the morphology of freshly fabricated Al NDs (inset) and after 6 months of air exposure, in order to better highlight the morphology change. The extinction spectra comprise the curves before and after aging to indoor air.

4. Conclusions

In this work, we present a study on the effect of MoO_x coating of Al nanodisks in a coupled configuration. The study covers the effect of the thin oxide on the far-field and near-field plasmonic features of the system, with a particular focus on the EM field confinement and enhancement within the nanogap. It was experimentally found that, by progressively coating Al dimers with large refractive index MoO_x, the extinction intensities and the near EM fields at the nanogaps were enhanced compared to bare dimers. Thanks to the conformality of the ALD oxide layer, a nanogap can be engineered in the sub-5-nm range without using extremely high resolution lithographic approaches.

Moreover, the beneficial effect of the MoO_x coating on the long term stability of the Al plasmonic nanostructures was also demonstrated. These results can be useful in a large number of applications involving Al plasmonic nanostructures, such as sensing, surface-enhanced Raman spectroscopy and catalysis.

Supplementary Materials: The following supporting information can be downloaded at: <https://www.mdpi.com/article/10.3390/photonics9080523/s1>, Figure S1: Simulated extinction spectra for Al dimers by progressively increasing the (a) MoO_x and (b) Al₂O₃ coatings on bared Al nanostructures (Al core/native Al₂O₃ shell dimers) up to 4 and 8 nm thick dielectric films, for s-pol and p-pol polarized excitation; Figure S2: Calculated two-dimensional near-field enhancement factor $|E/E_0|^2$ ($E_0 = 1$ V/m) maps (side view) for the bare (Al core/native Al₂O₃ shell dimers) and coated dimers with MoO_x layers (4 and 8 nm thick films). The maps are extracted at corresponding wavelengths of

maximum extinction peaks reported in Figure 2a (right panel), and at the nanoantenna height where the EM field is maximum; Figure S3: Simulated variations of field enhancement ($|E/E_0|^2$) values across the nanogap of the bare and coated dimers reported in Figure S2. The field enhancement was extracted at the nanoantenna height where the EM field is maximum; Figure S4: Percentage of EM field enhancement as function of the percentage of narrowed gap (by MoO_x ALD deposition), with respect to bare dimers for three initial nanogaps of 28, 12 and 5 nm.

Author Contributions: Conceptualization, D.L. and M.C.; methodology, D.L., M.M., G.B. and D.M.T.; software and validation, F.R., G.B. and M.E.; data curation, D.L., M.M., F.R., M.E., D.S., V.T. and M.C.; writing—original draft preparation, D.L., V.T. and M.C.; supervision, M.C.; project administration, A.P. and M.C.; funding acquisition, A.P. and M.C. All authors have read and agreed to the published version of the manuscript.

Funding: This research was partially funded by the national project “HYSPID” funded by National Research Council (CUP: B86C18000430006) and the regional project Innonetwork “IN-AIR” (CUP: B37H17004840007) funded by InnoVaPuglia.

Data Availability Statement: The data that support the findings of this study are available from the corresponding author upon reasonable request.

Acknowledgments: The authors are grateful to Iolena Tarantini (University of Salento) and Gianmichele Epifani (CNR NANOTEC) for technical support. In addition, we thank Sentech GmbH for technical support.

Conflicts of Interest: The authors declare no conflict of interest.

References

1. Simeone, D.; Tasco, V.; Esposito, M.; Manoccio, M.; Lorenzo, D.; Scuderi, M.; Luca, A.D.; Cabrini, S.; Passaseo, A.; Cuscunà, M. Near-Field Enhancement in Oxidized Close Gap Aluminum Dimers. *Nanotechnology* **2021**, *32*, 025305. [[CrossRef](#)] [[PubMed](#)]
2. Simeone, D.; Esposito, M.; Scuderi, M.; Calafiore, G.; Palermo, G.; De Luca, A.; Todisco, F.; Sanvitto, D.; Nicotra, G.; Cabrini, S.; et al. Tailoring Electromagnetic Hot Spots toward Visible Frequencies in Ultra-Narrow Gap Al/Al₂O₃ Bowtie Nanoantennas. *ACS Photonics* **2018**, *5*, 3399–3407. [[CrossRef](#)]
3. Gerislioglu, B.; Dong, L.; Ahmadvand, A.; Hu, H.; Nordlander, P.; Halas, N.J. Monolithic Metal Dimer-on-Film Structure: New Plasmonic Properties Introduced by the Underlying Metal. *Nano Lett.* **2020**, *20*, 2087–2093. [[CrossRef](#)] [[PubMed](#)]
4. Tian, L.; Wang, C.; Zhao, H.; Sun, F.; Dong, H.; Feng, K.; Wang, P.; He, G.; Li, G. Rational Approach to Plasmonic Dimers with Controlled Gap Distance, Symmetry, and Capability of Precisely Hosting Guest Molecules in Hotspot Regions. *J. Am. Chem. Soc.* **2021**, *143*, 8631–8638. [[CrossRef](#)]
5. Badilescu, S.; Raju, D.; Bathini, S.; Packirisamy, M. Gold Nano-Island Platforms for Localized Surface Plasmon Resonance Sensing: A Short Review. *Molecules* **2020**, *25*, 4661. [[CrossRef](#)]
6. Huang, Y.; Chen, Y.; Wang, L.-L.; Ringe, E. Small Morphology Variations Effects on Plasmonic Nanoparticle Dimer Hotspots. *J. Mater. Chem. C* **2018**, *6*, 9607–9614. [[CrossRef](#)]
7. Verre, R.; Maccaferri, N.; Fleischer, K.; Svedendahl, M.; Länk, N.O.; Dmitriev, A.; Vavassori, P.; Shvets, I.V.; Käll, M. Polarization Conversion-Based Molecular Sensing Using Anisotropic Plasmonic Metasurfaces. *Nanoscale* **2016**, *8*, 10576–10581. [[CrossRef](#)]
8. Shen, Z.; Su, L. Plasmonic Trapping and Tuning of a Gold Nanoparticle Dimer. *Opt. Express OE* **2016**, *24*, 4801–4811. [[CrossRef](#)]
9. Anker, J.N.; Hall, W.P.; Lyandres, O.; Shah, N.C.; Zhao, J.; Van Duyne, R.P. Biosensing with Plasmonic Nanosensors. *Nat. Mater.* **2008**, *7*, 442–453. [[CrossRef](#)] [[PubMed](#)]
10. Fusco, Z.; Bo, R.; Wang, Y.; Motta, N.; Chen, H.; Tricoli, A. Self-Assembly of Au Nano-Islands with Tuneable Organized Disorder for Highly Sensitive SERS. *J. Mater. Chem. C* **2019**, *7*, 6308–6316. [[CrossRef](#)]
11. Ray, N.J.; Yoo, J.-H.; Baxamusa, S.; Nguyen, H.T.; Elhadj, S.; Feigenbaum, E. Tuning Gold Nanoparticle Size with Fixed Interparticle Spacing in Large-Scale Arrays: Implications for Plasmonics and Nanoparticle Etching Masks. *ACS Appl. Nano Mater.* **2021**, *4*, 2733–2742. [[CrossRef](#)]
12. Li, W.; Camargo, P.H.C.; Lu, X.; Xia, Y. Dimers of Silver Nanospheres: Facile Synthesis and Their Use as Hot Spots for Surface-Enhanced Raman Scattering. *Nano Lett.* **2009**, *9*, 485–490. [[CrossRef](#)] [[PubMed](#)]
13. Czelej, K.; Colmenares, J.C.; Jabłczyńska, K.; Ćwieka, K.; Werner, Ł.; Gradoń, L. Sustainable Hydrogen Production by Plasmonic Thermophotocatalysis. *Catal. Today* **2021**, *380*, 156–186. [[CrossRef](#)]
14. Todisco, F.; Esposito, M.; Panaro, S.; De Giorgi, M.; Dominici, L.; Ballarini, D.; Fernández-Domínguez, A.I.; Tasco, V.; Cuscunà, M.; Passaseo, A.; et al. Toward Cavity Quantum Electrodynamics with Hybrid Photon Gap-Plasmon States. *ACS Nano* **2016**, *10*, 11360–11368. [[CrossRef](#)] [[PubMed](#)]
15. Ding, S.-Y.; You, E.-M.; Tian, Z.-Q.; Moskovits, M. Electromagnetic Theories of Surface-Enhanced Raman Spectroscopy. *Chem. Soc. Rev.* **2017**, *46*, 4042–4076. [[CrossRef](#)] [[PubMed](#)]

16. Huang, Y.; Zhou, Q.; Hou, M.; Ma, L.; Zhang, Z. Nanogap Effects on Near- and Far-Field Plasmonic Behaviors of Metallic Nanoparticle Dimers. *Phys. Chem. Chem. Phys.* **2015**, *17*, 29293–29298. [[CrossRef](#)]
17. Deng, L.; Zhai, Y.; Chen, Y.; Wang, N.; Huang, Y. Enhancing the Plasmonic Fields by a High Refractive Index Dielectric Coating for Surface Enhanced Spectroscopies. *J. Phys. D Appl. Phys.* **2019**, *52*, 43LT01. [[CrossRef](#)]
18. Deng, L.; Zhai, Y.; Chen, Y.; Wang, N.; Huang, Y. Enhancing Local Electric Fields at Plasmonic Nanogaps by Optimal Dielectric Coatings. *J. Phys. D Appl. Phys.* **2020**, *53*, 155103. [[CrossRef](#)]
19. Zhai, Y.; Deng, L.; Chen, Y.; Wang, N.; Huang, Y. Reducing the Loss of Electric Field Enhancement for Plasmonic Core–Shell Nanoparticle Dimers by High Refractive Index Dielectric Coating. *J. Phys. Condens. Matter* **2019**, *32*, 105001. [[CrossRef](#)]
20. Lin, T.-R.; Chang, S.-W.; Chuang, S.L.; Zhang, Z.; Schuck, P.J. Coating Effect on Optical Resonance of Plasmonic Nanobowtie Antenna. *Appl. Phys. Lett.* **2010**, *97*, 063106. [[CrossRef](#)]
21. Potts, S.E.; Keuning, W.; Langereis, E.; Dingemans, G.; van de Sanden, M.C.M.; Kessels, W.M.M. Low Temperature Plasma-Enhanced Atomic Layer Deposition of Metal Oxide Thin Films. *J. Electrochem. Soc.* **2010**, *157*, P66. [[CrossRef](#)]
22. George, S.M. Atomic Layer Deposition: An Overview. *Chem. Rev.* **2010**, *110*, 111–131. [[CrossRef](#)] [[PubMed](#)]
23. Cai, J.; Han, X.; Wang, X.; Meng, X. Atomic Layer Deposition of Two-Dimensional Layered Materials: Processes, Growth Mechanisms, and Characteristics. *Matter* **2020**, *2*, 587–630. [[CrossRef](#)]
24. Johnson, R.W.; Hultqvist, A.; Bent, S.F. A Brief Review of Atomic Layer Deposition: From Fundamentals to Applications. *Mater. Today* **2014**, *17*, 236–246. [[CrossRef](#)]
25. Puurunen, R.L. Surface Chemistry of Atomic Layer Deposition: A Case Study for the Trimethylaluminum/Water Process. *J. Appl. Phys.* **2005**, *97*, 121301. [[CrossRef](#)]
26. Langhammer, C.; Schwind, M.; Kasemo, B.; Zorić, I. Localized Surface Plasmon Resonances in Aluminum Nanodisks. *Nano Lett.* **2008**, *8*, 1461–1471. [[CrossRef](#)] [[PubMed](#)]
27. Gérard, D.; Gray, S.K. Aluminium Plasmonics. *J. Phys. D Appl. Phys.* **2014**, *48*, 184001. [[CrossRef](#)]
28. Nakamura, R.; Tokozakura, D.; Nakajima, H.; Lee, J.-G.; Mori, H. Hollow Oxide Formation by Oxidation of Al and Cu Nanoparticles. *J. Appl. Phys.* **2007**, *101*, 074303. [[CrossRef](#)]
29. Nguyen, L.; Hashimoto, T.; Zakharov, D.N.; Stach, E.A.; Rooney, A.P.; Berkels, B.; Thompson, G.E.; Haigh, S.J.; Burnett, T.L. Atomic-Scale Insights into the Oxidation of Aluminum. *ACS Appl. Mater. Interfaces* **2018**, *10*, 2230–2235. [[CrossRef](#)]
30. Yang, Y.; Kushima, A.; Han, W.; Xin, H.; Li, J. Liquid-Like, Self-Healing Aluminum Oxide during Deformation at Room Temperature. *Nano Lett.* **2018**, *18*, 2492–2497. [[CrossRef](#)]
31. Zhang, F.; Martin, J.; Plain, J. Long-Term Stability of Plasmonic Resonances Sustained by Evaporated Aluminum Nanostructures. *Opt. Mater. Express OME* **2019**, *9*, 85–94. [[CrossRef](#)]
32. Renard, D.; Tian, S.; Ahmadvand, A.; DeSantis, C.J.; Clark, B.D.; Nordlander, P.; Halas, N.J. Polydopamine-Stabilized Aluminum Nanocrystals: Aqueous Stability and Benzo[a]Pyrene Detection. *ACS Nano* **2019**, *13*, 3117–3124. [[CrossRef](#)]
33. Scuderi, M.; Esposito, M.; Todisco, F.; Simeone, D.; Tarantini, I.; De Marco, L.; De Giorgi, M.; Nicotra, G.; Carbone, L.; Sanvitto, D.; et al. Nanoscale Study of the Tarnishing Process in Electron Beam Lithography-Fabricated Silver Nanoparticles for Plasmonic Applications. *J. Phys. Chem. C* **2016**, *120*, 24314–24323. [[CrossRef](#)]
34. Roy, P.; Badie, C.; Claude, J.-B.; Barulin, A.; Moreau, A.; Lumeau, J.; Abbarchi, M.; Santinacci, L.; Wenger, J. Preventing Corrosion of Aluminum Metal with Nanometer-Thick Films of Al₂O₃ Capped with TiO₂ for Ultraviolet Plasmonics. *ACS Appl. Nano Mater.* **2021**, *4*, 7199–7205. [[CrossRef](#)]
35. Renard, D.; Tian, S.; Lou, M.; Neumann, O.; Yang, J.; Bayles, A.; Solti, D.; Nordlander, P.; Halas, N.J. UV-Resonant Al Nanocrystals: Synthesis, Silica Coating, and Broadband Photothermal Response. *Nano Lett.* **2021**, *21*, 536–542. [[CrossRef](#)] [[PubMed](#)]
36. Gromov, A.; Ilyin, A.; Förster-Barth, U.; Teipel, U. Characterization of Aluminum Powders: II. Aluminum Nanopowders Passivated by Non-Inert Coatings. *Propellants Explos. Pyrotech.* **2006**, *31*, 401–409. [[CrossRef](#)]
37. Shahravan, A.; Desai, T.; Matsoukas, T. Passivation of Aluminum Nanoparticles by Plasma-Enhanced Chemical Vapor Deposition for Energetic Nanomaterials. *ACS Appl. Mater. Interfaces* **2014**, *6*, 7942–7947. [[CrossRef](#)] [[PubMed](#)]
38. Abdulagatov, A.I.; Yan, Y.; Cooper, J.R.; Zhang, Y.; Gibbs, Z.M.; Cavanagh, A.S.; Yang, R.G.; Lee, Y.C.; George, S.M. Al₂O₃ and TiO₂ Atomic Layer Deposition on Copper for Water Corrosion Resistance. *ACS Appl. Mater. Interfaces* **2011**, *3*, 4593–4601. [[CrossRef](#)]
39. Potts, S.E.; Schmalz, L.; Fenker, M.; Díaz, B.; Światowska, J.; Maurice, V.; Seyeux, A.; Marcus, P.; Radnóczy, G.; Tóth, L.; et al. Ultra-Thin Aluminium Oxide Films Deposited by Plasma-Enhanced Atomic Layer Deposition for Corrosion Protection. *J. Electrochem. Soc.* **2011**, *158*, C132. [[CrossRef](#)]
40. Li, M.; Jin, Z.-X.; Zhang, W.; Bai, Y.-H.; Cao, Y.-Q.; Li, W.-M.; Wu, D.; Li, A.-D. Comparison of Chemical Stability and Corrosion Resistance of Group IV Metal Oxide Films Formed by Thermal and Plasma-Enhanced Atomic Layer Deposition. *Sci. Rep.* **2019**, *9*, 10438. [[CrossRef](#)]
41. Herzinger, C.M.; Johs, B.; McGahan, W.A.; Woollam, J.A.; Paulson, W. Ellipsometric Determination of Optical Constants for Silicon and Thermally Grown Silicon Dioxide via a Multi-Sample, Multi-Wavelength, Multi-Angle Investigation. *J. Appl. Phys.* **1998**, *83*, 3323–3336. [[CrossRef](#)]
42. Aspnes, D.E.; Studna, A.A. Dielectric Functions and Optical Parameters of Si, Ge, GaP, GaAs, GaSb, InP, InAs, and InSb from 1.5 to 6.0 eV. *Phys. Rev. B* **1983**, *27*, 985–1009. [[CrossRef](#)]
43. Malitson, I.H. Interspecimen Comparison of the Refractive Index of Fused Silica. *J. Opt. Soc. Am.* **1965**, *55*, 1205. [[CrossRef](#)]

44. Langereis, E.; Heil, S.B.S.; Knoop, H.C.M.; Keuning, W.; van de Sanden, M.C.M.; Kessels, W.M.M. In Situ Spectroscopic Ellipsometry as a Versatile Tool for Studying Atomic Layer Deposition. *J. Phys. D Appl. Phys.* **2009**, *42*, 073001. [[CrossRef](#)]
45. Mattinen, M.; King, P.J.; Khriachtchev, L.; Heikkilä, M.J.; Fleming, B.; Rushworth, S.; Mizohata, K.; Meinander, K.; Räsänen, J.; Ritala, M.; et al. Atomic Layer Deposition of Crystalline Molybdenum Oxide Thin Films and Phase Control by Post-Deposition Annealing. *Mater. Today Chem.* **2018**, *9*, 17–27. [[CrossRef](#)]
46. Haerberle, J.; Henkel, K.; Gargouri, H.; Naumann, F.; Gruska, B.; Arens, M.; Tallarida, M.; Schmeißer, D. Ellipsometry and XPS Comparative Studies of Thermal and Plasma Enhanced Atomic Layer Deposited Al₂O₃-Films. *Beilstein J. Nanotechnol.* **2013**, *4*, 732–742. [[CrossRef](#)]
47. McPeak, K.M.; Jayanti, S.V.; Kress, S.J.P.; Meyer, S.; Iotti, S.; Rossinelli, A.; Norris, D.J. Plasmonic Films Can Easily Be Better: Rules and Recipes. *ACS Photonics* **2015**, *2*, 326–333. [[CrossRef](#)]
48. Boidin, R.; Halenkovič, T.; Nazabal, V.; Beneš, L.; Němec, P. Pulsed Laser Deposited Alumina Thin Films. *Ceram. Int.* **2016**, *42*, 1177–1182. [[CrossRef](#)]
49. Sarkar, S.; Gupta, V.; Kumar, M.; Schubert, J.; Probst, P.T.; Joseph, J.; König, T.A.F. Hybridized Guided-Mode Resonances via Colloidal Plasmonic Self-Assembled Grating. *ACS Appl. Mater. Interfaces* **2019**, *11*, 13752–13760. [[CrossRef](#)]
50. Nordlander, P.; Oubre, C.; Prodan, E.; Li, K.; Stockman, M.I. Plasmon Hybridization in Nanoparticle Dimers. *Nano Lett.* **2004**, *4*, 899–903. [[CrossRef](#)]
51. Mertens, J.; Eiden, A.L.; Sigle, D.O.; Huang, F.; Lombardo, A.; Sun, Z.; Sundaram, R.S.; Colli, A.; Tserkezis, C.; Aizpurua, J.; et al. Controlling Subnanometer Gaps in Plasmonic Dimers Using Graphene. *Nano Lett.* **2013**, *13*, 5033–5038. [[CrossRef](#)] [[PubMed](#)]
52. McMahon, J.M.; Li, S.; Ausman, L.K.; Schatz, G.C. Modeling the Effect of Small Gaps in Surface-Enhanced Raman Spectroscopy. *J. Phys. Chem. C* **2012**, *116*, 1627–1637. [[CrossRef](#)]
53. Standridge, S.D.; Schatz, G.C.; Hupp, J.T. Toward Plasmonic Solar Cells: Protection of Silver Nanoparticles via Atomic Layer Deposition of TiO₂. *Langmuir* **2009**, *25*, 2596–2600. [[CrossRef](#)]
54. Bahk, Y.-M.; Kim, D.-S.; Park, H.-R. Large-Area Metal Gaps and Their Optical Applications. *Adv. Opt. Mater.* **2019**, *7*, 1800426. [[CrossRef](#)]
55. Xiang, Q.; Li, Z.; Zheng, M.; Liu, Q.; Chen, Y.; Yang, L.; Jiang, T.; Duan, H. Sensitive SERS Detection at the Single-Particle Level Based on Nanometer-Separated Mushroom-Shaped Plasmonic Dimers. *Nanotechnology* **2018**, *29*, 105301. [[CrossRef](#)]
56. Yang, Y.; Gu, C.; Li, J. Sub-5 nm Metal Nanogaps: Physical Properties, Fabrication Methods, and Device Applications. *Small* **2019**, *15*, 1804177. [[CrossRef](#)]
57. Duan, H.; Fernández-Domínguez, A.I.; Bosman, M.; Maier, S.A.; Yang, J.K.W. Nanoplasmonics: Classical down to the Nanometer Scale. *Nano Lett.* **2012**, *12*, 1683–1689. [[CrossRef](#)]
58. Barulin, A.; Claude, J.-B.; Patra, S.; Moreau, A.; Lumeau, J.; Wenger, J. Preventing Aluminum Photocorrosion for Ultraviolet Plasmonics. *J. Phys. Chem. Lett.* **2019**, *10*, 5700–5707. [[CrossRef](#)] [[PubMed](#)]
59. Vos, M.F.J.; Macco, B.; Thissen, N.F.W.; Bol, A.A.; Kessels, W.M.M. (Erwin) Atomic Layer Deposition of Molybdenum Oxide from (N^tBu)₂(NMe₂)₂Mo and O₂ Plasma. *J. Vac. Sci. Technol. A Vac. Surf. Films* **2016**, *34*, 01A103. [[CrossRef](#)]